



Structural and magnetic properties of $\text{Ca}_3\text{Mn}_{2-x}\text{Ru}_x\text{O}_7$ ($0 < x \leq 0.9$)J. Blasco ^{1,*}, J. A. Rodríguez-Velamazán,² J. L. García-Muñoz,³ V. Cuartero ^{1,4}, S. Lafuerza,¹ and G. Subías¹¹*Instituto de Nanociencia y Materiales de Aragón, Departamento de Física de la Materia Condensada, CSIC-Universidad de Zaragoza, C/Pedro Cerbuna 12, E-50009 Zaragoza, Spain*²*Institut Laue-Langevin, Grenoble Cedex 38042, France*³*Institut de Ciència de Materials de Barcelona, ICMA-B-CSIC, Campus UAB, 08193, Bellaterra, Spain*⁴*Departamento de Ciencia y Tecnología de Materiales y Fluidos, Universidad de Zaragoza, C/María de Luna 3, 50018, Zaragoza, Spain*

(Received 27 July 2022; accepted 16 September 2022; published 5 October 2022)

We here report on the study of the crystallographic and magnetic properties of layered perovskites $\text{Ca}_3\text{Mn}_{2-x}\text{Ru}_x\text{O}_7$ ($x \leq 0.9$). We observe a solid solution between Mn and Ru atoms in the whole series and all samples present the same orthorhombic structure independently of the Ru content. Different magnetic structures, depending on the Ru content in the sample, have been determined using neutron powder diffraction. For low Ru doping ($x \leq 0.1$), there is a dominant *G*-type antiferromagnetic ordering in the perovskite bilayers but, differently from undoped $\text{Ca}_3\text{Mn}_2\text{O}_7$, the magnetic moments are located on the *ab* plane. For higher Ru concentration ($x \geq 0.3$), the predominant *G*-type ordering is preserved along the *y* axis while an *A*-type component is developed along the *x* axis and its intensity increases as Ru content does. This component is characterized by a ferromagnetic ordering in the *a* direction of one of the Mn(Ru)O₆ layers, coupled antiferromagnetically with the neighbor Mn(Ru)O₆ layer within the same bilayer. The study of the macroscopic magnetic properties shows that ferromagneticlike correlations are enhanced with increasing Ru content as deduced from the shift to higher temperature of the onset of the magnetic transition temperature. The magnetic transitions take place in two steps. At higher temperatures (140–200 K), short-range magnetic correlations are established. Tiny spontaneous magnetization is observed in the hysteresis loops with small coercive field. At $T_N \approx 115$ –125 K, long-range antiferromagnetic ordering is developed. The ferromagnetic component remains with a strong increase of coercivity. We discuss in the paper the possible origins of this ferromagnetic contribution.

DOI: [10.1103/PhysRevB.106.134403](https://doi.org/10.1103/PhysRevB.106.134403)**I. INTRODUCTION**

Layered perovskites belonging to the Ruddlesden-Popper structure with double stacked MO_6 octahedra, $\text{A}_3\text{M}_2\text{O}_7$ (*A* = alkaline earth or rare earth; *M* = transition metal), have recently attracted much attention due to the predicted improper ferroelectricity [1]. The polarized state of these compounds arises from a combination of rotations and tilts of the MO_6 octahedra that stabilize a polar structure with space group $A2_1am$, a subgroup of the undistorted parent tetragonal structure with space group $I4/mmm$ in the high-temperature paraelectric phase [1]. This prediction was experimentally demonstrated in bulk crystals of $\text{Ca}_3\text{Ti}_2\text{O}_7$ and Sr-doped $\text{Ca}_3\text{Ti}_2\text{O}_7$ where switchable polarization at room temperature was found [2]. However, Ti^{4+} is a nonmagnetic ion, so much interest was focused on an isostructural compound like $\text{Ca}_3\text{Mn}_2\text{O}_7$ with a magnetic Mn^{4+} cation and promising expectations to develop multiferroic properties with magnetoelectric coupling [1,3]. The Mn moments undergo an antiferromagnetic (AFM) ordering [4] of *G* type at $T_N = 112$ K and the net magnetization exhibits a weak ferromagnetism below T_N which can be modulated by the electric field [3].

Despite the seemingly promising multiferroic-magnetoelectric properties of $\text{Ca}_3\text{Mn}_2\text{O}_7$, its electric and magnetic properties are not well understood so far. Measurements of the relative dielectric permittivity on polycrystalline samples suggest a possible ferroelectric (FE) transition in $\text{Ca}_3\text{Mn}_2\text{O}_7$ at $T_C \approx 240$ K [3], though a structural phase coexistence was detected for a large temperature range [3,5]. In particular, high-resolution diffraction measurements using both neutron and synchrotron radiation have revealed that the tetragonal phase first undergoes a transition into a nonpolar structure with space group *Acaa* that coexists with the low-temperature polar phase between 320 and 200 K [5]. As there is no group-subgroup relationship between *Acaa* and $A2_1am$ phases, the transition between them cannot be continuous [6]. However, a recent spectroscopic and crystallographic study on single crystals has disclosed a structural transition at about 400 K yielding a polar structure [7]. This study suggests a higher T_C for single crystals and a direct transition from the tetragonal phase into the $A2_1am$ one. Therefore, the sequence of structural transitions is still controversial and seems to depend on the type of specimen [5,7]. In spite of the polar ground state of $\text{Ca}_3\text{Mn}_2\text{O}_7$, no clear switchable FE polarization has been observed in this manganite at room temperature due to its significant conductivity [3], contrary to what happens in $\text{Ca}_3\text{Ti}_2\text{O}_7$, $\text{Sr}_3\text{Zr}_2\text{O}_7$, or $\text{Sr}_3\text{Sn}_2\text{O}_7$ [2,8,9]. In the meantime, a recent study using transmission electron microscopy has revealed

*jbc@unizar.es

a unique domain structure in the ground state of $\text{Ca}_3\text{Mn}_2\text{O}_7$ composed by a stacking of a and b domains along the c axis that prevents the polarization switching [10].

Different substitutions have been tested to improve the FE properties of this system. Most of them were focused on the A site by doping with Na, La, and Sr [6,11,12]. The tensile strain induced by these substitutions led to an increased symmetry of the unit cell that is detrimental for the development of electric polarization. Theoretical studies also suggest that a compressive strain induced by Ca substitution with Li leads to an increase [13] of T_N . However, samples have only been realized for small doping rates and the tiny increase in T_N is accompanied by the formation of oxygen vacancies favoring the presence of conducting electrons, which is negative for FE setups [14]. Only a few studies have been devoted to B -site substitution in $\text{Ca}_3\text{Mn}_2\text{O}_7$. In particular, the phase diagram of $\text{Ca}_3\text{Mn}_{2-x}\text{Ti}_x\text{O}_7$ indicates [7] that the FE transition temperature T_C linearly increases as Ti content does while T_N decreases and the AFM ordering vanishes before $x = 1$. More promising seems to be the B -site cosubstitution using Nb^{5+} together with a trivalent cation such as Al^{3+} or Fe^{3+} [15,16]. In both cases, ferroelectricity is improved and in the case of codoping with Fe^{3+} , a direct transition from tetragonal to polar phase with easier polarization switching is induced [16].

Overall, little attention has been paid to the possibility of enhancing the magnetism in this compound, which is a fundamental aspect for the applications of a multiferroic compound in sensing, spintronics, or high-performance information storage devices [17]. The aim of this work is to gain insights into alternative strategies to promote the magnetism of this system without affecting the electric polarization. For this purpose, we studied the $\text{Ca}_3\text{Mn}_{2-x}\text{Ru}_x\text{O}_7$ system because the magnetic Ru^{4+} -O- Mn^{4+} superexchange interaction has been proven to enhance ferromagnetism in simple perovskites [18,19]. In addition, $\text{Ca}_3\text{Ru}_2\text{O}_7$ adopts the same polar structure [20] as $\text{Ca}_3\text{Mn}_2\text{O}_7$ so a Mn/Ru solid solution is expected. It is noteworthy that $\text{Ca}_3\text{Ru}_2\text{O}_7$ has been described using the space group $Bb2_1m$ which transforms into $A2_1am$ by interchanging a and b axes.

II. EXPERIMENTAL SECTION

Polycrystalline $\text{Ca}_3\text{Mn}_{2-x}\text{Ru}_x\text{O}_7$ ($x = 0.05, 0.1, 0.3, 0.5, 0.7, 0.9$) samples were prepared by solid state reaction of Mn_2O_3 , CaCO_3 , and RuO_2 powders. The powders were calcined at 900 °C in air overnight. Then they were pressed into pellets and sintered at 1200 °C for 16 h in an oxygen current flow. The pellets were ground, repressed, and sintered at 1325 °C in oxygen for 16 h. The synthesis from stoichiometric amounts of the precursors always led to the occurrence of secondary phases identified as Ca_2MnO_4 , CaO , and perovskite whose content increases as the x value does. This is due to the high volatility of RuO_2 so that an excess of RuO_2 is necessary to achieve single phase compounds. Two procedures were used to incorporate the additional Ru, either weighing more starting RuO_2 (about 10%–15% in weight), or adding it in the intermediate steps. The amount is then estimated from the phase quantification of the x-ray

diffraction (XRD) patterns. In general, the second method yielded more reproducible samples.

The samples were characterized by powder XRD with a Rigaku D-Max system using $\text{Cu } K\alpha_{1,2}$ wavelengths. The chemical composition of the samples was tested by using the wavelength dispersive x-ray fluorescence spectrometry technique. Only single phase samples with the right chemical stoichiometry as determined by these techniques were used for the present study. Neutron powder diffraction (NPD) measurements were performed at the high-flux reactor of the ILL using the high-intensity powder diffractometer D1B with a detector angular range coverage $5^\circ \leq 2\theta \leq 128^\circ$, which is especially suited for magnetic structure determination. Two wavelengths were used, either $\lambda \approx 1.29 \text{ \AA}$ for the structural characterization at room temperature or $\lambda \approx 2.52 \text{ \AA}$ for the determination of the low-temperature magnetic structure. In the latter case, diffraction patterns were collected between 2 K and room temperature. Both XRD and NPD patterns were analyzed by the Rietveld method using the FULLPROF software package [21]. The schematic illustrations of the crystal structures and magnetic arrangements were obtained with the VESTA program [22].

Magnetic measurements were carried out between 2 and 350 K using a commercial superconducting quantum interference device (SQUID) magnetometer from Quantum Design.

III. RESULTS AND DISCUSSION

A. Crystal structure at room temperature

Neutron diffraction patterns were collected at room temperature (295 K) with $\lambda = 1.29 \text{ \AA}$ in order to study the evolution of the crystal structure along this series. They were refined using the same orthorhombic unit cell with $Bb2_1m$ space group (No. 36, standard setting $Cmc2_1$ with a being the long axis). This is the same space group reported for both parent compounds, $\text{Ca}_3\text{Mn}_2\text{O}_7$ and $\text{Ca}_3\text{Ru}_2\text{O}_7$ [4,20]. According to previous symmetry analysis [1], this space group is adopted by $A_3M_2O_7$ Ruddlesden-Popper phases as the small size of Ca^{2+} cations favors the MO_6 tilting following the $a^-a^-c^+$ tilt schema of Glazer's notation [23]. The $a^-a^-c^+$ tilt pattern is achieved by the simultaneous $a_0a_0c^+$ rotation and $a^-a^-c_0$ tilt, which in addition are coupled to a zone-center polar mode giving rise to the so-called trilinear coupling mechanism [24], a geometric mechanism able to induce improper ferroelectricity in a wide set of structures derived from perovskites such as Ruddlesden-Popper phases [25], Aurivillius phases [24], or double perovskites [26,27]. Our results clearly reveal that this hybrid coupling is fully operational in all $\text{Ca}_3\text{Mn}_{2-x}\text{Ru}_x\text{O}_7$ samples because they all have the same crystallographic structure.

We show in Fig. 1 the fits obtained for the neutron patterns of $x = 0.05$ and $x = 0.9$ samples (consult the Supplemental Material [28] for fits for the other compositions). The observed changes in the relative intensity of the diffraction peaks are mainly due to the large difference in neutron scattering lengths between Mn and Ru atoms, i.e., -3.73 and $+7.03$ fm, respectively [29]. The refined structural parameters are listed together with the reliability factors in Table I. An average temperature factor was refined for all atoms to avoid

TABLE I. Lattice parameters, atom fractional coordinates, average temperature factor, and reliability factors obtained from the Rietveld analysis of $\text{Ca}_3\text{Mn}_{2-x}\text{Ru}_x\text{O}_7$ compounds at 295 K. Errors in parentheses refer to the last significant digit and y coordinate of Ca(1) was fixed to set an origin. Ca1 and O1 are at the position $2a$, the rest of atoms are at $8b$.

Sample	$x = 0.05$	$x = 0.1$	$x = 0.3$	$x = 0.5$	$x = 0.9$
a (Å)	5.2731(3)	5.2865(4)	5.3220(3)	5.3472(3)	5.3878(4)
b (Å)	5.2664(3)	5.2794(4)	5.3176(3)	5.3487(3)	5.4066(4)
c (Å)	19.5021(8)	19.5022(9)	19.4912(11)	19.479(8)	19.4968(13)
V (Å ³)	541.59(5)	544.26(7)	551.61(6)	557.12(5)	567.94(7)
Ca1: x	0.2482(17)	0.2494(18)	0.2488(10)	0.2498(13)	0.2518(15)
y	0.0000	0.0000	0.0000	0.0000	0.0000
z	0	0	0	0	0
Ca2: x	0.2520(11)	0.2534(12)	0.2537(7)	0.2550(8)	0.2545(9)
y	0.0272(20)	0.0373(19)	0.0425(10)	0.0527(12)	0.0665(12)
z	0.1858(1)	0.1858(2)	0.1863(1)	0.1867(1)	0.1877(2)
Mn/Ru: x	0.2510(25)	0.2497(27)	0.2534(22)	0.2478(54)	0.2501(49)
y	0.0101(26)	0.0198(31)	0.0247(22)	0.0380(49)	0.0380(54)
z	0.4022(2)	0.4020(3)	0.4018(3)	0.4023(7)	0.4006(7)
O1: x	0.7954(9)	0.7965(12)	0.8053(7)	0.8082(9)	0.8151(10)
y	0.0114(27)	0.0271(31)	0.0274(16)	0.0362(20)	0.0496(20)
z	0	0	0	0	0
O2: x	0.2180(6)	0.2152(7)	0.2119(4)	0.2057(6)	0.1969(7)
y	0.0018(25)	0.0162(28)	0.0132(15)	0.0195(17)	0.0267(16)
z	0.3042(1)	0.3039(1)	0.3041(1)	0.3038(1)	0.3034(2)
O3: x	-0.0393(9)	-0.0375(9)	-0.0399(6)	-0.0410(7)	-0.0428(8)
y	0.2165(24)	0.2296(26)	0.2293(14)	0.2355(15)	0.2410(15)
z	0.4113(1)	0.4114(2)	0.4125(1)	0.4135(1)	0.4152(1)
O4: x	0.5354(9)	0.5384(10)	0.5381(9)	0.5397(7)	0.5419(7)
y	-0.2083(26)	-0.1950(27)	-0.1915(14)	-0.1837(16)	-0.1740(15)
z	0.3946(1)	0.3942(2)	0.3929(1)	0.3918(1)	0.3895(1)
B_{av} (Å ²):	0.57(2)	0.55(2)	0.58(2)	0.63(2)	0.65(2)
R_{wp} (%)	3.94	4.44	2.24	2.01	3.47
R_{B} (%)	2.26	2.18	1.62	2.99	2.32
χ^2	1.83	1.44	4.78	3.42	2.90

overparametrization. Despite this constraint, the fits are fairly good as can be seen in Fig. 1 and Table I. The calculated bond lengths and bond angles from these refinements are summarized in Table II. All compounds are isostructural but the unit cell volume increases with x , in agreement with Ru^{4+} ion (0.62 Å) substitution into the Mn^{4+} (0.53 Å) sites [30].

However, this change is not isotropic and, for instance, the b axis gets longer than the a axis as x increases, while the c axis expansion has a maximum and then decreases for $x = 0.9$. Accordingly, the interatomic distances of MO_6 octahedra ($M = \text{Mn}, \text{Ru}$; see Table II) increase in the $\text{Ca}_3\text{Mn}_{2-x}\text{Ru}_x\text{O}_7$ samples with increasing x . This trend is accompanied by a

TABLE II. Deduced bond lengths (Å) and bond angles (deg) for MO_6 octahedra ($M = \text{Mn}, \text{Ru}$), and BVS values for Mn and Ru from the Rietveld refinements at 295 K. O1 and O2 are apical oxygens while O3 and O4 are basal ones.

Sample	$x = 0.05$	$x = 0.1$	$x = 0.3$	$x = 0.5$	$x = 0.9$
M -O1	1.922(4)	1.927(6)	1.934(6)	1.930(16)	1.970(14)
M -O2	1.920(5)	1.923(7)	1.917(6)	1.934(16)	1.918(14)
M -O3	1.888(14)	1.890(19)	1.911(12)	1.884(27)	1.943(27)
M -O3	1.913(17)	1.908(20)	1.950(12)	1.972(28)	1.976(28)
M -O4	1.895(16)	1.907(19)	1.913(12)	1.970(27)	1.958(27)
M -O4	1.870(17)	1.881(12)	1.881(12)	1.883(28)	1.931(28)
$\langle M$ -O)	1.901	1.906	1.918	1.929	1.949
M -O1- M	166.0(4)	165.2(6)	163.4(5)	160.8(15)	159.2(13)
M -O3- M	158.5(13)	159.2(16)	157.1(10)	155(2)	154(2)
M -O4- M	162.1(14)	161.0(16)	160.5(10)	160(3)	158(2)
$\langle M$ -O- M)	162.2	161.8	160.3	158.6	157.1
BVS_{Mn}	4.03(6)	3.97(7)	3.85(4)	3.75(10)	3.53(9)
BVS_{Ru}	5.01(8)	4.94(9)	4.79(6)	4.66(13)	4.40(12)

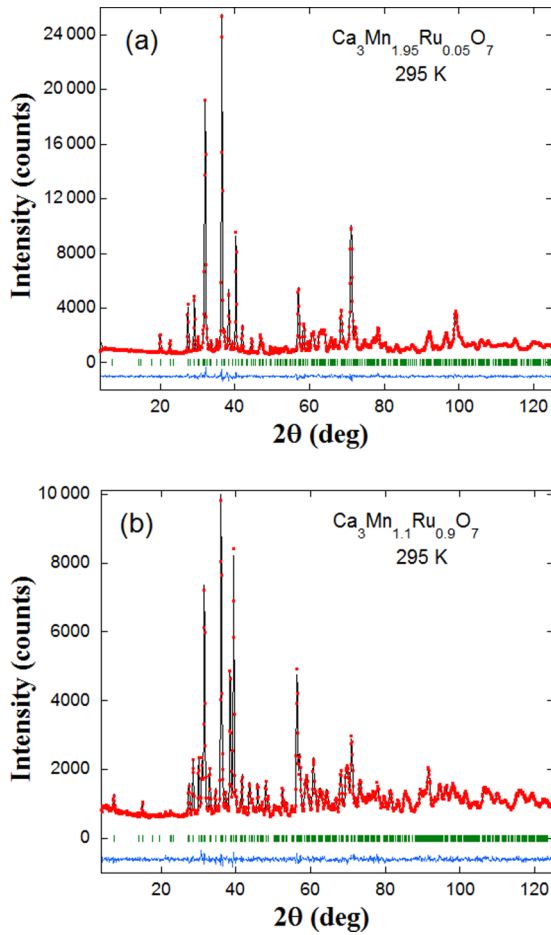


FIG. 1. Observed (points), calculated (full line), and difference (bottom line) neutron diffraction profiles for (a) $\text{Ca}_3\text{Mn}_{1.95}\text{Ru}_{0.05}\text{O}_7$ and (b) $\text{Ca}_3\text{Mn}_{1.1}\text{Ru}_{0.9}\text{O}_7$ at 295 K. The bars denote the allowed reflections.

decrease in the $M\text{-O-M}$ bond angles in agreement with an increase of MO_6 tilts to relieve the strain produced by the small Ca^{2+} size in this layered perovskite. Table II also shows the bond valence sum (BVS) values [31] for both cations. For samples with a small degree of substitution ($x \leq 0.1$), the coordination environment of Mn fits perfectly to a tetravalent cation. On the other hand, Ru is strongly overbonded. This indicates that Ru-O bonds are too short in the $\text{Ca}_3\text{Mn}_2\text{O}_7$ matrix and the RuO_6 octahedron is under compressive stress. As the degree of substitution progresses ($x \geq 0.3$), Ru is less overbonded while Mn begins to be underbonded; i.e., the compressive stress on RuO_6 is relieved while a tensile stress appears on MnO_6 . Therefore, the average distances obtained from the crystallographic structures evidence a balance between the steric requirements of Mn and Ru atoms.

B. Magnetic properties

Figure 2 shows the temperature scans of dc magnetization for $\text{Ca}_3\text{Mn}_{2-x}\text{Ru}_x\text{O}_7$ samples. The measurements were taken in a magnetic field of 500 Oe after zero field cooling (ZFC) and field cooling (FC) in the same field. The magnetic properties of this series can be divided into two groups. Samples with small Ru content ($x \leq 0.1$), shown in

Fig. 2(a), have similar properties to the parent compound, $\text{Ca}_3\text{Mn}_2\text{O}_7$ (magnetization curves are shown in the Supplemental Material [28]). These samples are characterized by a clear magnetic transition whose onset is at about 125 K and have a strong magnetic irreversibility between ZFC and FC conditions below $T_N \approx 115\text{--}120$ K, in agreement with similar features previously reported for $\text{Ca}_3\text{Mn}_2\text{O}_7$ [32–34]. The ZFC curves show a peak at T_N characteristic of an antiferromagnetic (AFM) transition with a weak ferromagnetic (FM) component. The FC curves, instead, are more typical of a FM transition. A peculiar property is the presence of a local maximum, T_{max} , in the $M(T)$ curve well above T_N which is observed in both ZFC and FC conditions, as can be seen in Fig. 2(a), suggesting that the magnetic transition is developed in two steps. This broad maximum has been ascribed to either short-range magnetic correlations [35] or quasi-two-dimensional (2D) magnetic fluctuations [33] above T_N in related layered perovskites. In this concentration range, T_{max} decreases as Ru content increases, achieving values of 155, 150, and 145 K for $x = 0, 0.05$, and 0.1 , respectively, i.e., a decrease rate of -100 K/ x . As Ru content in the samples increases further ($x \geq 0.3$), the magnetization of the samples is strongly enhanced at low temperatures and the magnetic transition becomes broader, overlapping the T_{max} feature that now is seen as a shoulder on the $M(T)$ curve [see Fig. 2(b)]. The occurrence of two inflection points is best visualized on the dM/dT curves [see Fig. 2(c)]. In these curves, T_N is observed as a sharp minimum between 115 K ($x = 0.9$) and 125 K ($x = 0.3$ and 0.5). A second minimum, denoted as T'_{max} for its resemblance to the T_{max} described in the $x \leq 0.1$ samples, is observed at higher temperatures. Its values range from 150 K (for $x = 0.3$) up to 200 K (for $x = 0.7$). Finally, T_{onset} marks the beginning of magnetic interactions upon cooling and above this temperature a normal paramagnetic behavior is observed for all samples. Magnetic irreversibility is preserved with similar features for these samples ($x \geq 0.3$), i.e., a peak in the ZFC branches and a FM-like transition in the FC curves [Fig. 2(b)]. Moreover, the onset of the magnetic correlations is shifted to higher temperatures with increasing Ru content. This result suggests a strengthening of the magnetic interactions due to Ru addition. Especially significant is the evolution of T'_{max} in Fig. 2(c). However, this enhancement of the magnetic properties seems to reach its maximum value for $x = 0.7$ since T_{onset} decreases again for $x = 0.9$ [see Fig. 2(c)].

Magnetic hysteresis loops were measured for all samples at 5 K between -50 and 50 kOe as can be seen in Fig. 3(a). All samples exhibit a weak ferromagnetism marked by the occurrence of hysteresis loops with small remanence as observed in the parent $\text{Ca}_3\text{Mn}_2\text{O}_7$ [3]. None of the samples reach magnetic saturation at 50 kOe. As Ru content increases, the remanence and coercivity in the hysteresis loops increase up to $x = 0.7$ and then decrease slightly for $x = 0.9$. The experimental remanence ranges between $0.002 \mu_B/\text{f.u.}$ ($x = 0.05$) and $0.008 \mu_B/\text{f.u.}$ ($x = 0.7$). We have also measured the loop for the $x = 0$ sample as a reference (see Supplemental Material) [28]. The experimental remanence was $0.002 \mu_B/\text{f.u.}$ which agrees with previous reports [34]. Therefore, Ru incorporation enhances the FM component which in any case is still rather weak. First principle calculations [1] gave a weak FM component of 0.18

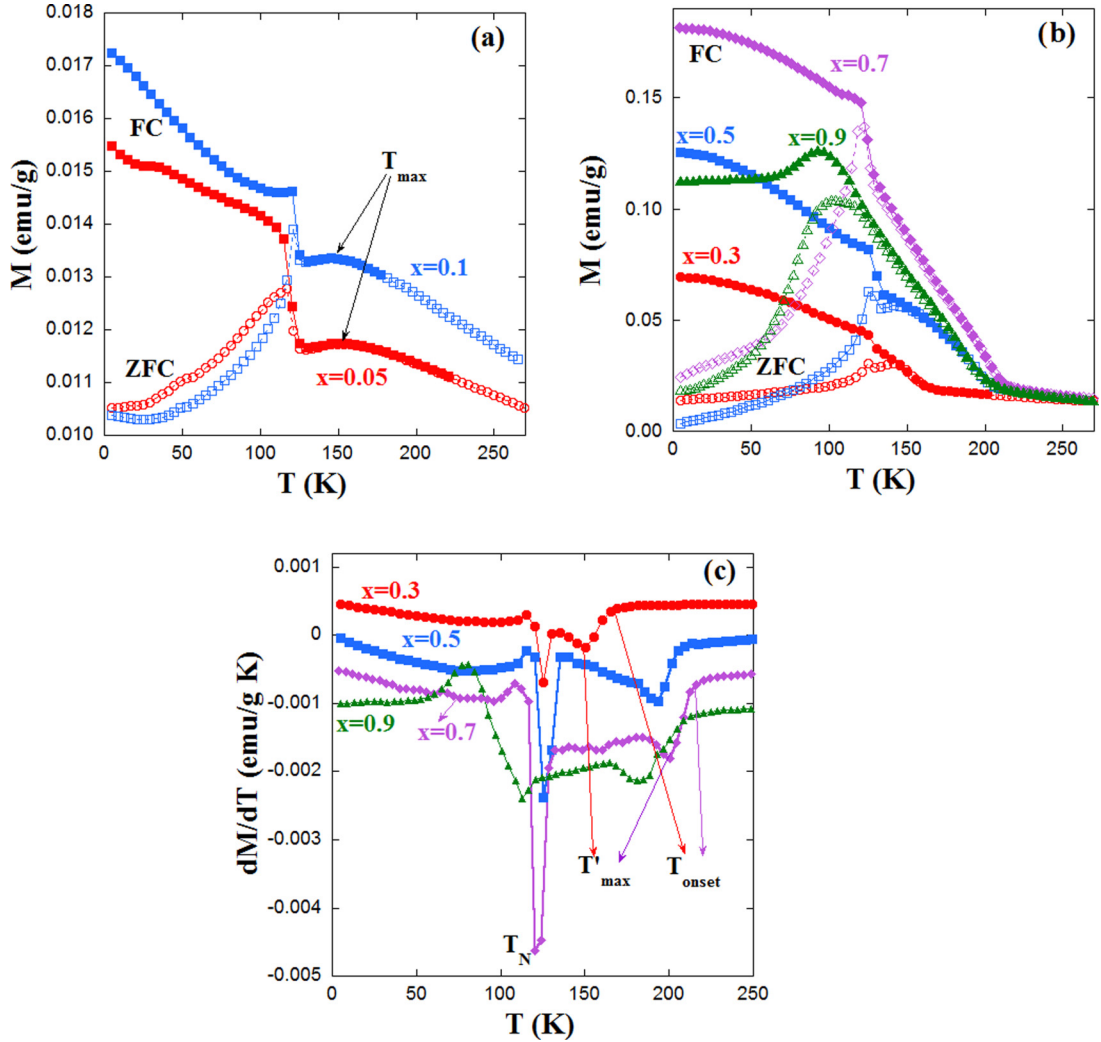


FIG. 2. Temperature dependence of magnetization in ZFC (open symbols) and FC (full symbols) conditions for (a) $\text{Ca}_3\text{Mn}_{1-x}\text{Ru}_x\text{O}_7$ ($x = 0.05$ and 0.1) and (b) the rest of the series ($0.3 \leq x \leq 0.9$) at a field of 500 Oe. (c) Derivative of magnetization vs temperature in FC conditions for $\text{Ca}_3\text{Mn}_{1-x}\text{Ru}_x\text{O}_7$ ($0.3 \leq x \leq 0.9$). The arrows for T'_{\max} and T_{onset} indicate the extreme values in these samples.

μ_B per unit cell (i.e., $0.09 \mu_B/\text{f.u.}$) for $\text{Ca}_3\text{Mn}_2\text{O}_7$ which is an order of magnitude higher than that obtained from isothermal measurements.

We can clearly distinguish two different behaviors in the magnetic hysteresis loops of this series. For samples with small Ru contents ($x \leq 0.1$), the $M(H)$ curve is linear in the $[-20 \text{ kOe} \leq H \leq 20 \text{ kOe}]$ range, and then the slope is increased above 20 kOe (or below -20 kOe), as can be seen in Fig. 2(b) for $\text{Ca}_3\text{Mn}_{1.9}\text{Ru}_{0.1}\text{O}_7$. This phenomenon is seen in a wide range of temperatures and suggests the onset of changes in the magnetic ordering induced by the external magnetic field. Similar hysteresis loops were observed in $\text{Ca}_3\text{Mn}_2\text{O}_7$ and a Na-doped compound [11]. For samples with Ru content $x \geq 0.3$, the hysteresis loops show spontaneous magnetization and a linear contribution at high fields. Figure 3(c) shows the temperature dependence of magnetic loops at selected temperatures for $\text{Ca}_3\text{Mn}_{1.3}\text{Ru}_{0.7}\text{O}_7$. Spontaneous magnetization is also observed above T_N but below T'_{\max} [see Fig. 2(c)]. Therefore, the tiny FM contribution is extended up to temperatures close to T'_{\max} and the linear behavior at high fields may be ascribed to either a paramagnetic (PM) phase above

T_N or an AFM one below T_N . Above T_{onset} , the temperature dependence of PM magnetization obeys the Curie-Weiss law for all samples. The fits can be found in the Supplemental Material [28] and the best fit values are summarized in Table III, including also the parent compound for comparison. From these data, the presence of strong AFM correlations in

TABLE III. Magnetic parameters (Curie and Weiss constants from the law $\chi = C/[(T-\theta)]$ and calculated effective paramagnetic moments compared to the theoretical ones (spin only) from Mn^{4+} and low-spin Ru^{4+} .

Sample (x)	C (emu K/mol)	θ (K)	ρ_{eff} ($\mu_B/\text{f.u.}$)	ρ_{theor} ($\mu_B/\text{f.u.}$)
0	6.88	-644.6	7.41	5.37
0.05	6.63	-645	7.28	5.34
0.1	5.29	-401.7	6.50	5.31
0.3	3.78	-121.4	5.50	5.19
0.5	3.33	-57.7	5.16	5.06
0.7	3.04	-7.9	4.93	4.93
0.9	2.75	10.3	4.69	4.79

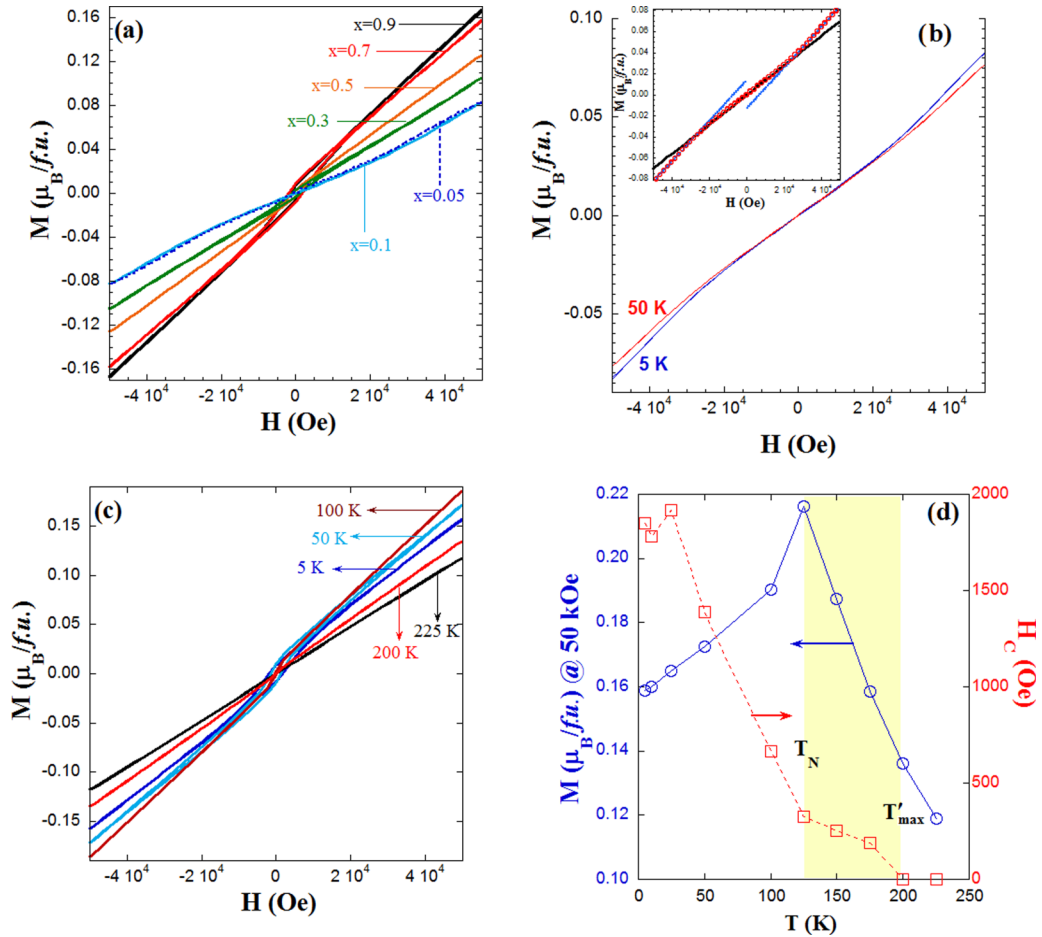


FIG. 3. (a) Magnetic hysteresis loops at 5 K for $\text{Ca}_3\text{Mn}_{2-x}\text{Ru}_x\text{O}_7$ (x is indicated for each curve). (b) $M(H)$ loops for $\text{Ca}_3\text{Mn}_{1.9}\text{Ru}_{0.1}\text{O}_7$ at 5 K (blue line) and 50 K (red line). Inset: The same loop at 5 K with linear fits between $-20 \text{ kOe} \leq H \leq 20 \text{ kOe}$ (black solid line) and from ± 30 to $\pm 50 \text{ kOe}$ (blue broken lines). (c) $M(H)$ loops for $\text{Ca}_3\text{Mn}_{1.3}\text{Ru}_{0.7}\text{O}_7$ at selected temperatures between 5 and 225 K. (d) Temperature dependence of coercivity and magnetization at 50 kOe for the hysteresis loops of $\text{Ca}_3\text{Mn}_{1.3}\text{Ru}_{0.7}\text{O}_7$.

the PM region is deduced for the parent compound ($x = 0$) and samples with low Ru doping. As Ru content increases, the initially negative Weiss constant increases and even changes its sign for $x = 0.9$ indicating an increase in FM correlations. The effective paramagnetic moments (ρ_{eff}) decrease as Ru content does. This suggests that Mn^{4+} ($S = 3/2$) is replaced by low-spin Ru^{4+} ($S = 1$). However, the calculated values (spin-only contribution) are well below the experimental ones for $x \leq 0.1$ samples and agree better for $x \geq 0.3$ (compare ρ_{eff} and ρ_{theor} in Table III). This behavior might be related to the magnitude of AFM correlations mentioned above because the largest deviation is observed in the parent compound without Ru atoms.

The temperature dependences of both the coercive field and the magnetization value at 50 kOe of the hysteresis loops from Fig. 3(c) are displayed in Fig. 3(d) for $\text{Ca}_3\text{Mn}_{1.3}\text{Ru}_{0.7}\text{O}_7$, representative of the set of samples with $0.3 \leq x \leq 0.9$. The coercive field achieves values around 1850(70) Oe below 25 K, but above this temperature, the coercivity decreases with increasing temperature until the FM contribution vanishes at about T'_{max} . Moreover, the decreasing rate of coercivity slows down at $T_N \approx 125$ K. A different behavior is observed for the magnetization value at 50 kOe; it increases until T_N and then it decreases following the behavior expected for a dominant

PM contribution. Similar behavior is observed for the rest of the $x \geq 0.3$ samples where T_N is almost constant while T'_{max} fluctuates between 150 and 200 K [see Fig. 2(c)].

C. Magnetic ground state

In order to gain insights into the magnetic properties of these samples, neutron diffraction patterns were measured down to 10 K using $\lambda = 2.52 \text{ \AA}$ to be more sensitive to the magnetic contribution. The comparison of neutron patterns above and below the magnetic anomalies was very clarifying.

1. $\text{Ca}_3\text{Mn}_{0.95}\text{Ru}_{0.05}\text{O}_7$ and $\text{Ca}_3\text{Mn}_{0.9}\text{Ru}_{0.1}\text{O}_7$

Both samples exhibit similar magnetic contribution at low temperature in their NPD patterns. Figure 4(a) compares the neutron patterns of $\text{Ca}_3\text{Mn}_{0.9}\text{Ru}_{0.1}\text{O}_7$ at three representative temperatures ($10 \text{ K} < T_N$; $T_N < 135 \text{ K} < T_{\text{max}}$; $285 \text{ K} > T_{\text{max}}$) focused on the region where the most important magnetic contribution is observed. New magnetic peaks are noticeable below T_N as can be seen from the indexation performed in the pattern at 10 K [Fig. 4(a)]. They can be indexed either following the propagation vector $\mathbf{k} = 0$ (Γ point) or the vector corresponding to the Y point in the first Brillouin zone, $\mathbf{k}' = [0, 0, 1]$. The magnetic reflection conditions are different

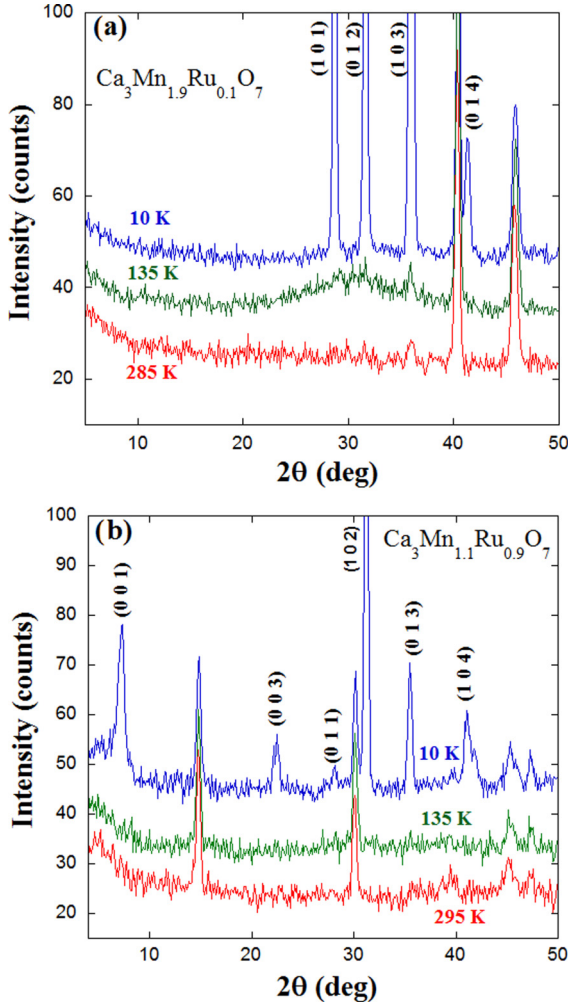


FIG. 4. Comparison of the neutron diffraction patterns collected at three selected temperatures for (a) $\text{Ca}_3\text{Mn}_{1.9}\text{Ru}_{0.1}\text{O}_7$ and (b) $\text{Ca}_3\text{Mn}_{1.1}\text{Ru}_{0.9}\text{O}_7$. The region with the most important magnetic contribution is emphasized and the magnetic peaks have been indexed following the propagation vector $\mathbf{k} = 0$ in panel (a) and $\mathbf{k}' = [0, 0, 1]$ in panel (b). Patterns are shifted upward for comparison.

in both cases. These are $(0, 1, \text{even})$ and $(1, 0, \text{odd})$ for the first case but $(0, 1, \text{odd})$ and $(1, 0, \text{even})$ for the second one. The quasitetragonal crystal structure of this compound prevents an unambiguous identification of the correct propagation vector by NPD. The occurrence of spontaneous magnetization in the hysteresis loops suggests a FM component which is only possible for $\mathbf{k} = 0$ [4]. The magnetic peaks of Fig. 4(a) are the same as those identified [4] in $\text{Ca}_3\text{Mn}_2\text{O}_7$ but their relative intensities are different. This suggests a common magnetic structure, G type, but a different orientation of the magnetic moments. The neutron patterns collected between T_N and T_{max} show magnetic diffuse scattering as can be seen in the pattern measured at 135 K [Fig. 4(a)]. This is evidenced as a broad bump centered at the positions where sharp magnetic peaks are observed at 10 K. This result agrees with short-range magnetic correlations between T_N and T_{max} . As indicated in Ref. [4], the occurrence of diffuse scattering in reflections with nonzero l index indicates that these correlations are not exclusively 2D.

TABLE IV. Magnetic irreducible representations, associated k points, magnetic space groups (number and BNS symbol), and magnetic structure within a bilayer (Bertaut's notation) for Γ and Y points for the crystal structure of $\text{Ca}_3\text{Mn}_{2-x}\text{Ru}_x\text{O}_7$ samples with space group $Bb2_1m$.

mIrrep	k point	Magnetic group	Magnetic structure ^a
$m\Gamma_1$	(0, 0, 0)	36.172 $Bb2_1m$	$A_x G_y C_z$
$m\Gamma_2$	(0, 0, 0)	36.176 $Bb'2_1m'$	$C_x F_y A_z$
$m\Gamma_3$	(0, 0, 0)	36.175 $Bb'2_1m'$	$G_x A_y F_z$
$m\Gamma_4$	(0, 0, 0)	36.174 $Bb2_1m'$	$F_x C_y G_z$
mY_1	(0, 0, 1)	26.76P _B $b2_1m$	$A_x G_y C_z$
mY_2	(0, 0, 1)	33.154 $P_{Bn}2_1a$	$C_x F_y A_z$
mY_3	(0, 0, 1)	31.133 $P_{Bn}2_1m$	$G_x A_y F_z$
mY_4	(0, 0, 1)	29.109P _B $b2_1a$	$F_x C_y G_z$

^a $m\Gamma_n$ and mY_n ($n = 1-4$) have the same type of magnetic structure in a particular bilayer but the interaction between neighboring bilayers is of opposite sign (see examples in the Supplemental Material [28]).

In order to solve the magnetic arrangement, a symmetry analysis was performed using the program ISODISTORT [36] to explore the magnetic irreducible representations (mIrreps) for the nuclear cell with $Bb2_1m$ symmetry. This strategy was used previously to solve magnetic structures in related perovskites [37]. The search was initially limited to Γ and Y -points and the results are summarized in Table IV. According to the magnetic peaks observed in Fig. 4(a), the most suitable magnetic structure belongs to the Irrep $m\Gamma_1$ (or mY_3) which led to G -type magnetic arrangements with the moments perpendicular to crystallographic planes defined by the main magnetic peaks. This corresponds to a G_y magnetic structure following Bertaut's notation [38] (or G_x using the mY_3 model). Although this model is the one from Table IV that best fits the experimental pattern, the result is not good enough as can be seen in Fig. 5(a), with a reliability factor $R_{\text{mag}} = 15.2\%$. The lack of intensity in the $(0, 1, \text{even})$ refined peaks clearly implies the need of a G component in the x direction. We have made the fit with a $G_x G_y$ model and the fit improves considerably, obtaining a good $R_{\text{mag}} = 2.5\%$ [see Fig. 5(b)]. The refined magnetic moment is $[1.09(2), 2.12(2), 0]$ and the occurrence of a $G_x G_y$ magnetic ordering implies that the true magnetic structure should arise from the superposition of two mIrreps, $m\Gamma_1 \oplus m\Gamma_3$, and the corresponding magnetic space group should be Bm (No. 8.32). It is noteworthy that an equally good fit is obtained using the combination $mY_1 \oplus mY_3$ (magnetic space group Pm , No. 6.23) with a similar result by exchanging the previous x and y components of the magnetic moment. We believe that the first model is more plausible because it allows the existence of a FM component along the c axis that would be in better agreement with the spontaneous magnetization observed in macroscopic measurements and previous calculations [1]. Nevertheless, our attempts to refine this component were unsuccessful, obtaining small values with large standard deviations, which suggests that this small FM component is below the sensitivity limit of the NPD technique. This is in agreement with the low value of magnetic remanence observed in these compounds [see magnetic hysteresis loops of Fig. 3(a)].

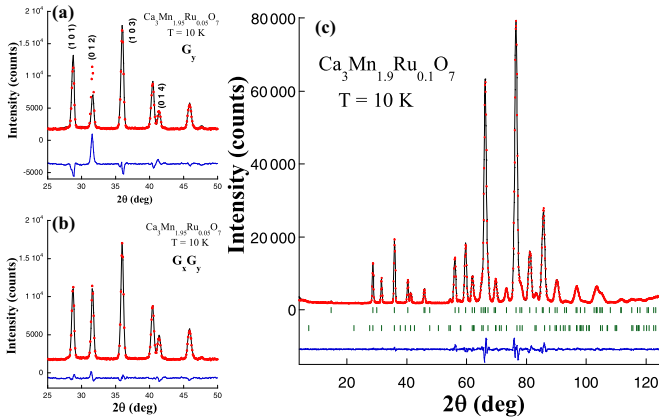


FIG. 5. Observed (red points), calculated (black line) and difference (bottom blue line) neutron diffraction profiles focused on the magnetic contribution for the $\text{Ca}_3\text{Mn}_{0.95}\text{Ru}_{0.05}\text{O}_7$ sample at 10 K using (a) a G_y -type arrangement (from $m\Gamma_1$) and (b) a $G_x G_y$ magnetic structure (from $m\Gamma_1 \oplus m\Gamma_3$). (c) Observed (red points), calculated (black line), and difference (bottom blue line) neutron diffraction profiles for $\text{Ca}_3\text{Mn}_{1.9}\text{Ru}_{0.1}\text{O}_7$ sample at 10 K using a $G_x G_y$ -type magnetic structure ($\mathbf{k} = 0$). The bars denote the allowed reflections for the nuclear (top row) and magnetic (bottom row) phases.

Similar results were found in $\text{Ca}_3\text{Mn}_{1.9}\text{Ru}_{0.1}\text{O}_7$, where a good fit is obtained using the same model as can be seen in Fig. 5(c). Here the refined magnetic moment was $[0.60(3), 2.27(2), 0]$ suggesting that an increase in Ru content tends to place the magnetic moments closer to one of the crystallographic axes in the ab plane (the b axis for the $m\Gamma_1 \oplus m\Gamma_3$ model). The refined parameters are summarized in Table V. When these values are compared with published results for the parent compound $\text{Ca}_3\text{Mn}_2\text{O}_7$ [4], a surprising finding is detected regarding the orientation of the magnetic moments. A small replacement of Mn by Ru is enough to rearrange the ordered magnetic moments from the long c axis ($x = 0$) [4] to within the ab plane as we find for $x = 0.05$.

TABLE V. Refined unit cell parameters, magnetic moments, and reliability factors for $\text{Ca}_3\text{Mn}_{2-x}\text{Ru}_x\text{O}_7$ samples. The magnetic space group used in the refinement is also indicated using the Belov-Neronova-Smirnova (BNS) notation.

Sample	$x = 0.05$	$x = 0.1$	$x = 0.3$	$x = 0.5$	$x = 0.7$	$x = 0.9$
Unit cell:						
a (Å)	5.2644(5)	5.2768(5)	5.3079(3)	5.3308(4)	5.3520(5)	5.3678(3)
b (Å)	5.2567(5)	5.2704(5)	5.3067(3)	5.3389(3)	5.3697(4)	5.4030(3)
c (Å)	19.4765(16)	19.4870(15)	19.4897(11)	19.4814(11)	19.4617(13)	19.4550(9)
V (Å ³)	534.48(9)	541.95(9)	548.97(6)	554.46(7)	559.30(8)	564.24(5)
Magn. SG:						
No.	8.32	8.32	26.76	26.76	26.76	26.76
BNS	Bm	Bm	$P_B b 2_1 m$	$P_B b 2_1 m$	$P_B b 2_1 m$	$P_B b 2_1 m$
μ_x ($\mu_B/\text{at.}$)	1.09(2)	0.58(3)	0.14(2)	0.27(1)	0.43(1)	0.59(1)
μ_y ($\mu_B/\text{at.}$)	2.12(29)	2.31(2)	2.31(1)	2.23(1)	2.06(2)	1.85(1)
$[\mu]$ ($\mu_B/\text{at.}$)	2.38(2)	2.38(2)	2.32(2)	2.25(1)	2.10(2)	1.94(1)
Type	$(G_x, G_y, 0)$	$(G_x, G_y, 0)$	$(A_x, G_y, 0)$	$(A_x, G_y, 0)$	$(A_x, G_y, 0)$	$(A_x, G_y, 0)$
R_{wp} (%)	4.6	3.4	2.7	2.9	3.4	2.8
R_B (%)	1.1	1.1	1.1	1.1	1.7	1.4
R_{mag} (%)	2.5	1.9	2.9	3.4	4.7	4.8
χ^2	5.5	2.5	3.0	5.0	7.0	1.8

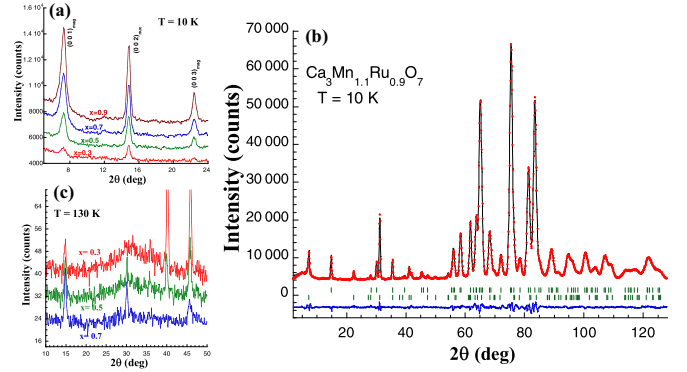


FIG. 6. (a) Detail of the neutron patterns at low angle for $\text{Ca}_3\text{Mn}_{2-x}\text{Ru}_x\text{O}_7$ ($0.3 \leq x \leq 0.9$) samples at 10 K. (b) Observed (red points), calculated (black line), and difference (bottom blue line) neutron diffraction profiles for the $\text{Ca}_3\text{Mn}_{1.1}\text{Ru}_{0.9}\text{O}_7$ sample at 10 K using a $A_x G_y$ -type magnetic structure ($\mathbf{k}' = [0, 0, 1]$). The bars denote the allowed reflections for the nuclear (top row) and magnetic (bottom row) phases. (c) Comparison of the neutron patterns of $\text{Ca}_3\text{Mn}_{2-x}\text{Ru}_x\text{O}_7$ ($x = 0.3, 0.5, \text{ and } 0.7$) samples measured at 130 K and focused on the region showing the diffuse magnetic scattering above T_N . Patterns are shifted upward for comparison.

2. $\text{Ca}_3\text{Mn}_{2-x}\text{Ru}_x\text{O}_7$ with $0.3 \leq x \leq 0.9$ samples

Figure 4(b) compares the neutron patterns of $\text{Ca}_3\text{Mn}_{1.1}\text{Ru}_{0.9}\text{O}_7$ at similar representative temperatures as the previous $\text{Ca}_3\text{Mn}_{0.9}\text{Ru}_{0.1}\text{O}_7$ sample. The nuclear and magnetic reflections of this composition are significantly different from the $x = 0.1$ patterns in Fig. 4(a). The changes in the nuclear part are due to the increase in Ru content as mentioned above. Regarding the pattern at 10 K, new magnetic peaks indexed as $(0, 0, l)$ are clearly noticeable in addition to the ones observed in the previous samples. These new magnetic peaks begin to appear in the neutron pattern of the $x = 0.3$ sample and their intensity increases with increasing Ru content as can be seen in Fig. 6(a).

This reveals that A - and G -type components coexist in the magnetic arrangement of $\text{Ca}_3\text{Mn}_{1.1}\text{Ru}_{0.9}\text{O}_7$ and the moments mainly lie on the ab plane. Moreover, the occurrence of $(0, 0, l)$ magnetic peaks excludes the $m\Gamma_n$ Irreps. From the data in Table IV, only the magnetic structure from mY_1 yielded satisfactory results as can be seen in Fig. 6(b) for $x = 0.9$. The magnetic structure is then A_xG_y with a refined moment of $[0.59(6), 1.85(1), 0]$ and $R_{\text{mag}} = 4.7\%$. In this model, there is no net magnetization per unit cell. In order to account for the small spontaneous magnetization observed by macroscopic measurements [see Fig. 3(c)], the only possibility is a FM component along the c axis. In this way, we have explored the combination of two Irreps, $mY_1 \oplus m\Gamma_3$, to get the $A_xG_yF_z$ magnetic structure. The resulting magnetic space group is $Pn'2_1m$ (No. 31.126) with two nonequivalent sites for Mn(Ru) atoms in the magnetic unit cell. The refinement using this model yields similar reliability factors without any improvement and the value for the FM component is 0.1(4); i.e., again the technique is not sensitive to such a small FM component. Therefore, the A_xG_y model was chosen to refine the magnetic structure of all $\text{Ca}_3\text{Mn}_{2-x}\text{Ru}_x\text{O}_7$ with $0.3 \leq x \leq 0.9$ samples. The refined parameters can be seen in Table V.

Another interesting feature, shown in Fig. 4(b) for $x = 0.9$, is the lack of short-range magnetic correlations in the neutron pattern collected between T_N and T'_{max} compared to the $x = 0.1$ sample [Fig. 4(a)]. This disappearance of the diffuse magnetic scattering occurs continuously as Ru content increases as can be seen in Fig. 6(c). It is still very significant in the sample with $x = 0.3$. It decreases considerably for the sample with $x = 0.5$ and is practically null for $\text{Ca}_3\text{Mn}_{1.3}\text{Ru}_{0.7}\text{O}_7$.

D. Magnetic phase diagram

NPD has revealed important changes in the magnetic ground state of $\text{Ca}_3\text{Mn}_{2-x}\text{Ru}_x\text{O}_7$ samples induced by Ru doping. These changes are not driven by any change in the crystalline structure as all compounds adopt the same B -centered orthorhombic cell and minor changes are observed in the temperature dependence of the lattice parameters across the magnetic transition (see Supplemental Material [28]). Therefore, the changes in the magnetic exchange interactions should play an active role when Ru substitutes for Mn. According to the expected superexchange magnetic interactions in mixed oxides of Mn and Ru with perovskite structure [39], the $\text{Mn}^{4+}\text{-O-Mn}^{4+}$ interaction is AFM. Therefore, G -type AFM ordering is observed in [4] $\text{Ca}_3\text{Mn}_2\text{O}_7$ and also in CaMnO_3 [40]. For the other end member of the series, $\text{Ca}_3\text{Ru}_2\text{O}_7$, one would expect t_{2g} FM and e_g AFM superexchange interactions [39]. This compound displays a range of magnetic arrangements depending on temperature and applied magnetic field [41]. At zero field, it develops an AFM ordering at $T_N = 56$ K and then a spin reorientation coupled to a metal-insulator transition at 46 K [42]. Regarding $\text{Mn}^{4+}\text{-O-Ru}^{4+}$ magnetic interaction, controversial works on the resulting magnetic ordering are found in the literature. The signs of the superexchange interactions are identical to that of $\text{Ru}^{4+}\text{-O-Ru}^{4+}$, which implies competitive interactions whose strength would depend on structural details, mainly the $M\text{-O-M}$ bond angle. For bond angles close to 180° , the weak

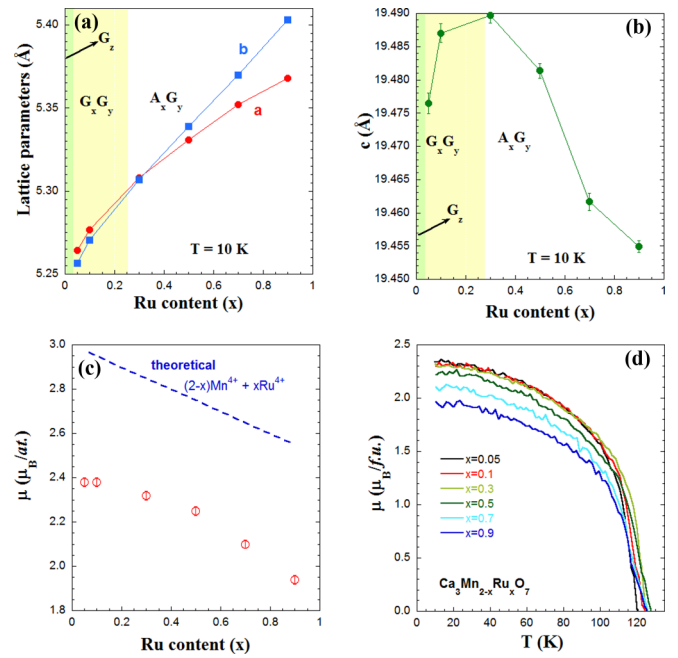


FIG. 7. Evolution of lattice parameters with the Ru content for $\text{Ca}_3\text{Mn}_{2-x}\text{Ru}_x\text{O}_7$ samples in (a) the ab plane, and (b) the c axis. (c) Refined magnetic moments (circles) compared to the expected values (broken line) from the addition of Mn^{4+} and low-spin Ru^{4+} cations. (d) Temperature dependence of the refined magnetic moments for $\text{Ca}_3\text{Mn}_{2-x}\text{Ru}_x\text{O}_7$ samples.

e_g AFM superexchange interaction would be reinforced, but as this angle decreases and moves away from 180° , the t_{2g} FM superexchange interaction gets stronger. Several works have reported that Ru doping induces FM in manganites rich in Mn^{4+} [18,19,43,44]. These experimental results would suggest an enhancement of the t_{2g} FM superexchange interaction. However, spectroscopic measurements using x-ray absorption and magnetic circular dichroism on epitaxial thin films of $\text{CaMn}_{1-x}\text{Ru}_x\text{O}_3$ have revealed that the spin moments of Mn^{4+} and Ru^{4+} are aligned in antiparallel directions, suggesting that the AFM coupling between Mn^{4+} and Ru^{4+} leads to a ferrimagnetic ground state [45].

Figures 7(a) and 7(b) show the relationship between the lattice parameters at 10 K and the magnetic ground state. The undoped compound has a G_z -type AFM structure [4]. For low Ru doping ($x \leq 0.1$), the magnetic structure becomes the G_xG_y type and is accompanied by an expansion of the three lattice parameters. For high Ru content ($x \geq 0.3$), the magnetic structure turns into A_xG_y type and while the ab plane keeps on expanding, the trend in the c axis changes and it starts to contract. In addition, the relationship in the a and b axes changes, with $b > a$, and this difference increases as the Ru content does. The incorporation of the large Ru^{4+} ions into the Mn^{4+} sites produces two effects (see Table II): an increase of the structural distortion (a decrease of the $M\text{-O-M}$ bond angles) and the occurrence of Ru-O-Mn and Ru-O-Ru magnetic interactions. For low Ru doping, the decrease of the $M\text{-O-M}$ bond angle is stronger in the ab plane, which can reinforce the t_{2g} AFM interactions (Mn-O-Mn) in this plane, inducing a spin reorientation from the c axis to the

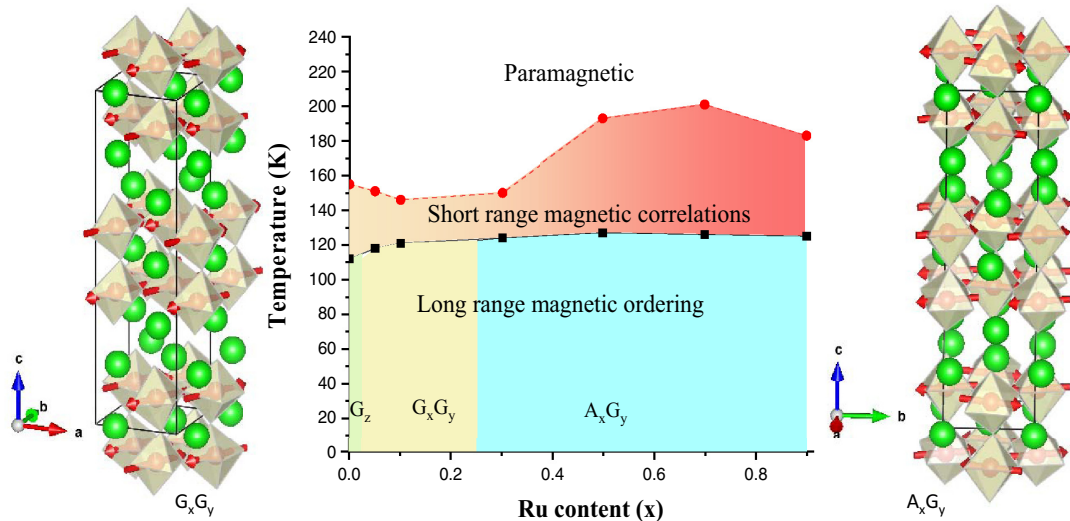


FIG. 8. Magnetic phase diagram for $\text{Ca}_3\text{Mn}_{2-x}\text{Ru}_x\text{O}_7$ series (middle) and magnetic structures for $\text{Ca}_3\text{Mn}_{1.95}\text{Ru}_{0.05}\text{O}_7$, ($\mathbf{k} = 0$) and $\text{Ca}_3\text{Mn}_{1.1}\text{Ru}_{0.9}\text{O}_7$ (right, $\mathbf{k}' = [0, 0, 1]$). Lines are guides for the eyes. Black squares stand for experimental T_N while red circles indicate T_{\max} ($x \leq 0.1$) and T'_{\max} ($x \geq 0.3$).

ab plane. For high Ru doping, the M - O - M angles decrease coupled to an increase of Ru- O -Ru FM interactions, leading to FM interactions in the ab plane resulting in the A_xG_y -type ordering.

Figure 7(c) compares the refined magnetic moment at 10 K to the expected values for the weighted sum of Mn^{4+} and Ru^{4+} moments. Qualitatively, the refined magnetic moments decrease as Mn^{4+} ($S = 3/2$) spins are replaced by Ru^{4+} ($S = 1$) ones. However, the experimental values are well below the theoretical ones indicating that the samples are not fully polarized. This may be a sign of the presence of competitive magnetic interactions and magnetic inhomogeneities as found in related systems [18]. Figure 7(d) shows the temperature dependence of the ordered magnetic moments for all samples. All the curves have a similar behavior and the ordered magnetic moment tends to zero in a temperature range between 120 and 125 K for all samples. This indicates that T_N barely changes with x in this range of doping. This contrasts with the $M(T)$ curves where an increase in the magnetic transition temperature with x is observed [compare Fig. 2(b) to Fig. 7(d)]. Clearly, the latter increase should be ascribed to the small FM contribution, not visible in NPD, as previously noticed. This difference between magnetization measurements and NPD may suggest that the FM contribution is due to magnetic inhomogeneities but the strong change in the coercive field of the hysteresis loops at T_N [see Fig. 3(d)] indicates that this FM component has an intrinsic character. Similar features were reported for the simple perovskite system $\text{CaMn}_{1-x}\text{Ru}_x\text{O}_3$ but here coexistence of G -type AFM and FM phases leads to a phase separated ground state [19]. In addition, short-range FM correlations are found above the long-range ordering temperature in $\text{CaMn}_{1-x}\text{Ru}_x\text{O}_3$, suggesting that short-range magnetic correlations are common in Ru-doped manganites and therefore they can be expected for the present bilayer manganite system. In fact, magnetic diffuse scattering associated to short-range AFM correlations is clearly noticeable in the NPD patterns for $x \leq 0.5$. For

these samples, strong AFM interactions in the PM region are inferred from the strong negative values of the Weiss constant (see Table III). For $x \geq 0.7$, the AFM correlations are weakened and even the Weiss constant changes its sign to positive for $x = 0.9$ indicating a prevalence of FM correlations in this case. The finding of diffuse magnetic scattering associated to short-range FM correlations would be hardly visible in NPD since this weak contribution should appear in the base of strong nuclear diffraction peaks. Based on these arguments, we propose the phase diagram shown in Fig. 8 for the $\text{Ca}_3\text{Mn}_{2-x}\text{Ru}_x\text{O}_7$ series. T_{\max} (or T'_{\max}) has been taken as the onset of short-range magnetic correlations and T_N as the onset of the long-range magnetic ordering. We have included T_N and T_{\max} points for the parent compound from previous works [11,32]. While T_N remains almost constant with x , the temperature at which short-range correlations appear increases with x up to $x = 0.7$ and then, it decreases again. The magnetic structures of $\text{Ca}_3\text{Mn}_{1.95}\text{Ru}_{0.05}\text{O}_7$ and $\text{Ca}_3\text{Mn}_{1.1}\text{Ru}_{0.9}\text{O}_7$ have also been included in Fig. 8 as representative examples of the magnetic arrangements found in this series.

IV. CONCLUSIONS

We have synthesized the layered perovskites $\text{Ca}_3\text{Mn}_{2-x}\text{Ru}_x\text{O}_7$ ($x \leq 0.9$). NPD shows single phase, chemical homogeneity, and the same crystal structure (with space group $Bb2_1m$) independently of the Ru content. The study of their macroscopic magnetic properties clearly reveals that FM is enhanced with respect to undoped $\text{Ca}_3\text{Mn}_2\text{O}_7$ by incorporating Ru into the Mn sites. This is manifested by the occurrence of spontaneous magnetization in the hysteresis loops with an increasing remanence upon Ru doping, and higher onsets of the magnetic transition temperature in the $M(T)$ curves. NPD reveals that all samples exhibit long-range magnetic order at similar temperatures ($T_N \approx 120$ – 125 K) and above T_N , short-range AFM correlations are clearly noticeable for $x \leq 0.5$ up to $T_{\max} \approx 140$ – 190 K depending on the Ru

content. The long-range magnetic ordering in all samples is mainly AFM. Accordingly, the FM enhancement seems to be concentrated in the region with short-range magnetic correlations above T_N . At high temperature, the magnetization curves of all samples obey the Curie-Weiss law, which unveils magnetic correlations whose sign changes from AFM in the low-doping samples to FM for $x = 0.9$. Isothermal measurements reveal a tiny spontaneous magnetization above T_N and the hysteresis loops have small coercive fields that experience a huge increase at T_N . This result suggests an intrinsic FM component but NPD could not detect it unambiguously because it is hard to distinguish between a magnetic inhomogeneity (majority AFM phase with a minority FM phase) and canting of the AFM phase. In this way, further experiments by means of either neutron diffraction in single crystals (if available) or x-ray magnetic circular dichroism measurements are desirable in order to determine the origin of the FM components and the exact magnetic coupling between Mn and Ru atoms.

Finally, NPD data have allowed a deeper knowledge of the magnetic arrangement in this system. Distinct AFM phases have been found depending on Ru content. Small doping concentration of Ru ($x = 0.05$) is enough to change the magnetic

structure of the undoped compound from G_z type into $G_x G_y$, i.e., a spin reorientation of 90° . Further increase in Ru concentration induces the formation of an $A_x G_y$ -type magnetic structure where in-plane FM interactions in individual layers are present in the x direction. These changes seem to be related to variations in the balance of competitive magnetic interactions induced by the replacement of Mn by Ru. As Ru^{4+} is larger than Mn^{4+} , the tilts of MO_6 octahedra are increased to relieve the structural strain. This favors t_{2g} superexchange interactions and the spins are oriented in the ab plane. As Ru content increases, the t_{2g} FM interaction ($\text{Ru}^{4+}\text{-O-Ru}^{4+}$) favors the appearing of the A_x component.

ACKNOWLEDGMENTS

The authors would like to acknowledge the use of Servicio General de Apoyo a la Investigación from Universidad de Zaragoza. For financial support, we thank the Spanish Ministerio de Economía y Competitividad [Projects No. RTI2018-098537-B-C22 and No. RTI2018-098537-B-C21, cofunded by ERDF from EU, the “Severo Ochoa” Programme (FUTURE (CEX2019-000917) and Diputación General de Aragón (Project No. E12-17R, RASMIA)]. We thank the ILL for the beamtime allocation under Experiment No. 5-31-2788.

-
- [1] N. A. Benedek and C. J. Fennie, *Phys. Rev. Lett.* **106**, 107204 (2011).
- [2] Y. S. Oh, X. Luo, F. T. Huang, Y. Wang, and S. W. Cheong, *Nat. Mater.* **14**, 407 (2015).
- [3] M. Liu, Y. Zhang, L.-F. Lin, L. Lin, S. Yang, X. Li, Y. Wang, S. Li, Z. Yan, X. Wang, X.-G. Li, S. Dong, and J.-M. Li, *Appl. Phys. Lett.* **113**, 022902 (2018).
- [4] M. V. Lobanov, M. Greenblatt, E. N. Caspi, J. D. Jorgensen, D. V. Sheptyakov, B. H. Toby, C. E. Botez, and P. W. Stephens, *J. Phys.: Condens. Matter* **16**, 5339 (2004).
- [5] M. S. Senn, A. Bombardi, C. A. Murray, C. Vecchini, A. Scherillo, X. Luo, and S. W. Cheong, *Phys. Rev. Lett.* **114**, 035701 (2015).
- [6] M. S. Senn, C. A. Murray, X. Luo, L. Wang, F.-T. Huang, S.-W. Cheong, A. Bombardi, C. Ablitt, A. A. Mostofi, and N. C. Bristowe, *J. Am. Chem. Soc.* **138**, 5479 (2016).
- [7] S. Liu, H. Zhang, S. Ghose, M. Balasubramanian, Z. Liu, S. G. Wang, Y.-S. Chen, B. Gao, J. Kim, S.-W. Cheong, and T. A. Tyson, *Phys. Rev. B* **99**, 224105 (2019).
- [8] S. Yoshida, K. Fujita, H. Akamatsu, O. Hernandez, A. S. Gupta, F. G. Brown, H. Padmanabhan, A. S. Gibbs, T. Kuge, R. Tsuji, S. Murai, J. M. Rondinelli, V. Gopalan, and K. Tanaka, *Adv. Funct. Mater.* **28**, 1801856 (2018).
- [9] Y. Wang, F.-T. Huang, X. Luo, B. Gao, and S.-W. Cheong, *Adv. Mater.* **29**, 1601288 (2017).
- [10] B. Gao, F.-T. Huang, Y. Wang, J.-W. Kim, L. Wang, S.-J. Lim, and S.-W. Cheong, *Appl. Phys. Lett.* **110**, 222906 (2017).
- [11] S. Li, S. Wang, Y. Lu, C. Zhang, X. Yang, J. Gao, D. Li, Y. Zhu, and W. Liu, *AIP Advances* **8**, 015009 (2018).
- [12] L. Ruiz-González, D. González-Merchante, R. Cortés-Gil, J. M. Alonso, J. L. Martínez, and A. Hernando, *Chem. Mater.* **27**, 1397 (2015).
- [13] A. I. Apostolov, I. N. Apostolova, and J. M. Weselinowa, *Phase Transitions* **94**, 705 (2021).
- [14] X. Zhang, W. Liu, Y. Han, C. Huang, P. Wu, W. Zhou, J. Gao, G. Rao, and S. Wang, *J. Mater. Chem. C* **5**, 7011 (2017).
- [15] B. H. Zhang, Z. Z. Hu, B. H. Chen, X. Q. Liu, and X. M. Chen, *J. Appl. Phys.* **128**, 054102 (2020).
- [16] B. H. Chen, T. L. Sun, L. Y. Wei, X. Q. Liu, W. Wen, H. Tian, J. Y. Li, and X. M. Chen, *J. Am. Ceram. Soc.* **104**, 4000 (2021).
- [17] R. Ramesh and N. A. Spaldin, *Nat. Mater.* **6**, 21 (2007).
- [18] B. Raveau, A. Maignan, C. Martin, R. Mahendiran, and M. Hervieu, *J. Solid State Chem.* **151**, 330 (2000).
- [19] A. I. Shames, E. Rozenberg, C. Martin, A. Maignan, B. Raveau, G. André, and G. Gorodetsky, *Phys. Rev. B* **70**, 134433 (2004).
- [20] Y. Yoshida, S.-I. Ikeda, H. Matsuhata, N. Shirakawa, C. H. Lee, and S. Katano, *Phys. Rev. B* **72**, 054412 (2005).
- [21] J. Rodríguez-Carvajal, *Physica B (Amsterdam)* **192**, 55 (1993).
- [22] K. Momma and F. Izumi, *J. Appl. Cryst.* **44**, 1272 (2011).
- [23] A. M. Glazer, *Acta Crystallogr., Sect. A* **31**, 756 (1975).
- [24] I. Etxeberria, J. M. Pérez-Mato, and P. Boullay, *Ferroelectrics* **401**, 17 (2010).
- [25] N. A. Benedek, J. M. Rodinelli, H. Djani, P. Ghosez, and P. Lightfoot, *Dalton Trans.* **44**, 10543 (2015).
- [26] J. Blasco, G. Subías, J. L. García-Muñoz, F. Fauth, and J. García, *J. Phys. Chem C* **125**, 19467 (2021).
- [27] J. Blasco, J. A. Rodríguez-Velamazán, G. Subías, J. L. García-Muñoz, J. Stankiewicz, and J. García, *Acta Mater.* **176**, 53 (2019).
- [28] See Supplemental Material at <http://link.aps.org/supplemental/10.1103/PhysRevB.106.134403> for details about Rietveld fits of NPD patterns at 295 and 10 K, temperature dependence of the refined lattice parameters, magnetization curve for the undoped compound ($\text{Ca}_3\text{Mn}_2\text{O}_7$), Curie-Weiss fits of $M^{-1}(T)$ curves,

- and schematic representations of different types of magnetic orderings ascribed either to Γ or Y points.
- [29] V. F. Sears, *Neutron News* **3**, 26 (1992).
- [30] R. D. Shannon, *Acta Crystallogr., Sect. A* **32**, 751 (1976).
- [31] W. H. Zachariasen, *J. Less Common Met.* **62**, 1 (1978).
- [32] M. V. Lobanov, S. Li, and M. Greenblatt, *Chem. Mater.* **15**, 1302 (2003).
- [33] I. D. Fawcett, E. Kim, M. Greenblatt, M. Croft, and L. A. Bendersky, *Phys. Rev. B* **62**, 6485 (2000).
- [34] P. Sahlot and A. M. Awasthi, *J. Magn. Magn. Mater.* **493**, 165732 (2020).
- [35] M. E. Lines, *Phys. Rev.* **164**, 736 (1967).
- [36] B. J. Campbell, H. T. Stokes, D. E. Tanner, and D. M. Hatch, ISODISPLACE: A web-based tool for exploring structural distortions, *J. Appl. Crystallogr.* **39**, 607 (2006) (available at ISOTROPY Software Suite, iso.byu.edu).
- [37] J. Blasco, J. A. Rodríguez-Velamazán, J. García, G. Subías, C. Piquer, V. Cuartero, M.C. Sánchez, and J. Stankiewicz, *Phys. Rev. B* **98**, 104422 (2018).
- [38] E. F. Bertaut, *Acta Crystallogr., Sect. A* **24**, 217 (1968).
- [39] M. F. Liu, Z. Z. Du, Y. L. Xie, X. Li, Z. B. Yan, and J.-M. Liu, *Sci. Rep.* **5**, 9922 (2015).
- [40] E. O. Wollan and W. C. Koehler, *Phys. Rev.* **100**, 545 (1955).
- [41] S. McCall, G. Cao, and J. E. Crow, *Phys. Rev. B* **67**, 094427 (2003).
- [42] W. Bao, Z. Q. Mao, Z. Qu, and J. W. Lynn, *Phys. Rev. Lett.* **100**, 247203 (2008).
- [43] C. L. Lu, X. Chen, S. Dong, K. F. Wang, H. L. Cai, J.-M. Liu, D. Li, and Z. D. Zhang, *Phys. Rev. B* **79**, 245105 (2009).
- [44] A. Maignan, C. Martin, M. Hervieu, and B. Raveau, *Solid State Commun.* **117**, 377 (2001).
- [45] K. Terai, K. Yoshii, Y. Takeda, S. I. Fujimori, Y. Saitoh, K. Ohwada, T. Inami, T. Okane, M. Arita, K. Shimada, H. Namatame, M. Taniguchi, K. Kobayashi, M. Kobayashi, and A. Fujimori, *Phys. Rev. B* **77**, 115128 (2008).